

Far- and Near-Field Channel Measurements and Characterization in the Terahertz Band Using a Virtual Antenna Array

Yiqin Wang, Shu Sun, and Chong Han, *Senior Member, IEEE*

Abstract—Extremely large-scale antenna array (ELAA) technologies consisting of ultra-massive multiple-input-multiple-output (UM-MIMO) or reconfigurable intelligent surfaces (RISs), are emerging to meet the demand of wireless systems in sixth-generation and beyond communications for enhanced coverage and extreme data rates up to Terabits per second. For ELAA operating at Terahertz (THz) frequencies, the Rayleigh distance expands, and users are likely to be located in both far-field (FF) and near-field (NF) regions. On one hand, new features like NF propagation and spatial non-stationarity need to be characterized. On the other hand, the transition of properties near the FF and NF boundary is worth exploring. In this paper, a complete experimental analysis of far- and near-field channel characteristics using a THz virtual antenna array is provided based on measurement of the multi-input-single-output channel with the virtual uniform planar array (UPA) structure of at most 4096 elements. In particular, non-linear phase change is observed in the NF, and the Rayleigh criterion regarding the maximum phase error is verified. Then, a new cross-field path loss model is proposed, which characterizes the power change at antenna elements in the UPA and is compatible with both FF and NF cases.

I. INTRODUCTION

While the lower part of the millimeter-wave (mmWave) frequency band (30-100 GHz) have been officially adopted in fifth-generation (5G) communications, sixth-generation (6G) is expected to explore higher frequency bands. Among candidate spectrum bands, the Terahertz (THz) band (0.1-10 THz, including the higher part of the mmWave band up to 300 GHz) is anticipated to address the spectrum scarcity and capacity limitations of current wireless systems. However, THz wave peculiarities, such as the narrow beam and strong path loss, constrain the transmission distance and signal coverage. In light of enormous spatial multiplexing and beamforming gain, ultra-massive multiple-input-multiple-output (UM-MIMO) and reconfigurable intelligent surfaces (RISs) that form extremely large-scale antenna array (ELAA) systems become a special interest for THz as they effectively increase the communication range and enhance the capacity in THz wireless communications [1].

Yiqin Wang is with Terahertz Wireless Communications (TWC) Laboratory, Shanghai Jiao Tong University, China (Email: wangyiqin@sjtu.edu.cn).

Shu Sun is with Department of Electronic Engineering and the Cooperative Medianet Innovation Center (CMIC), Shanghai Jiao Tong University, China (Email: shusun@sjtu.edu.cn).

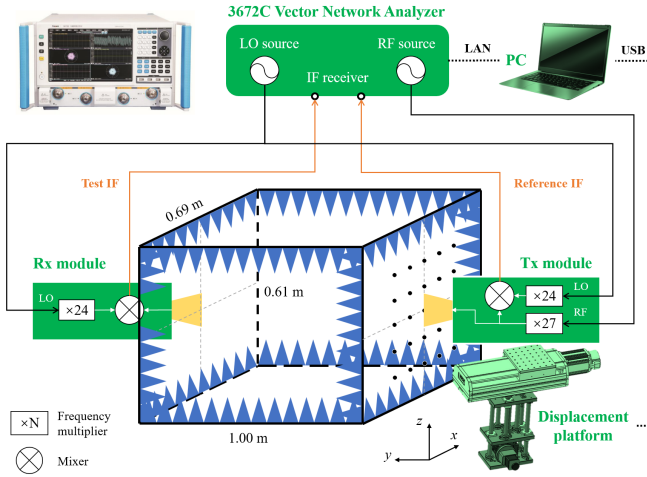
Chong Han is with Terahertz Wireless Communications (TWC) Laboratory, also with Department of Electronic Engineering and the Cooperative Medianet Innovation Center (CMIC), Shanghai Jiao Tong University, China (Email: chong.han@sjtu.edu.cn).

Especially, thanks to the small wavelength of THz waves, electrically large-scale arrays with reasonable physical dimension becomes realistic. However, for ELAA equipped with hundreds or thousands of antennas and high THz frequencies, features like near-field (NF) propagation and spatial non-stationarity arise and bring new challenges to channel modeling and characterization [2], [3]. In wireless communications, the electromagnetic (EM) radiation field is divided into the far-field (FF) region and the radiative NF region¹, typically by the boundary called Rayleigh distance [4], which is proportional to the square of array aperture and the carrier frequency. In THz ELAA systems, the Rayleigh distance increases as compared with lower frequency bands, and users are likely to be located in the NF region. First, the planar wavefront model fails in the NF region, where the phase value along antenna elements cannot be approximated by a linear change. Besides, in the NF region within the Rayleigh distance, the Friis' free-space path loss (FSPL) model is also no longer accurate [2], [5], [6].

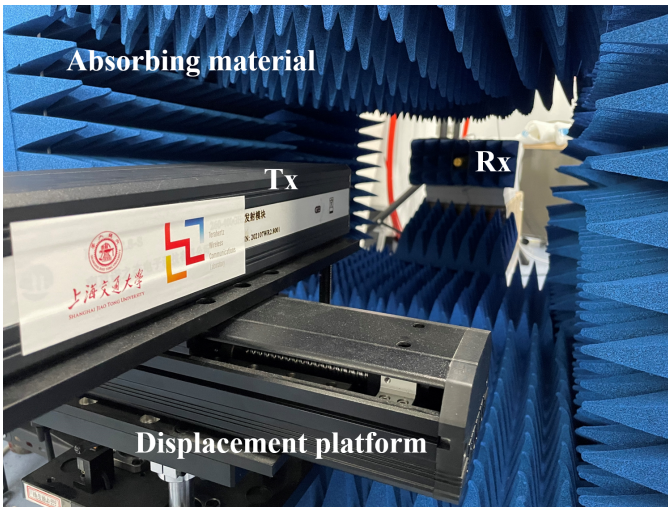
Till date, spherical wave propagation [7]–[15] and non-stationarity [16]–[19] have been analytically modeled, which are used to improve beamforming technologies on large-scale antenna arrays. Nevertheless, experimental characterization of NF effects is rare [20]–[22], let alone in the THz band. To fill this research gap, in this paper, we provide a complete analysis of hybrid far- and near-field channel characteristics in the THz band based on measurement using a virtual antenna array (VAA). Specifically, we carry out wideband THz channel measurements of the multi-input-single-output (MISO) system with the uniform planar array (UPA) structure. Channels from 256, 1024, and 4096 elements in the UPA are investigated. In the static environment, VAA is free of mutual coupling and represents the ideal case of the actual antenna array. In light of the measurement results, we elaborate the variation of properties, i.e., path loss and phase, of the line-of-sight (LoS) ray across elements in the UPA, in both FF and NF cases. First, a new cross-field path loss model is proposed, which characterizes the power change at antenna elements in the UPA and is compatible with both FF and NF cases. Then, the Rayleigh criterion, which distinguishes NF and FF in terms of the maximum phase error, is verified.

The remainder of this paper is organized as follows. The wideband THz virtual antenna array measurement is intro-

¹The near-field region is subdivided into reactive NF and radiative NF. Since EM waves in the reactive NF are induced fields and do not set off from the antenna, we only refer to the radiative NF in this article.



(a) The diagram of the MISO measuring system.



(b) The measurement scenario.

Fig. 1: Overview of the MISO measurement.

duced in Sec. II. We then analyze channel measurement results in Sec. III. Finally, the paper is concluded in Sec. IV.

II. CHANNEL MEASUREMENT CAMPAIGN

In this section, we introduce the vector network analyzer (VNA)-based THz MISO channel measurement platform, and describe the far-and-near-field measurement conducted in a small anechoic chamber wrapped by absorbing materials.

A. Channel Measurement System

The THz MISO channel measurement system is composed of three parts, as shown in Fig. 1(a), including the computer (PC) as the control platform, the displacement platform, and the measuring platform.

The measuring platform consists of THz transmitter (Tx) and receiver (Rx) modules and the Ceyear 3672C VNA. The VNA generates radio frequency (RF) and local oscillator (LO) sources. The RF signal is multiplied by 27 to reach the carrier frequencies. The LO signal is multiplied by 24. As designed,

TABLE I: Parameters of the measurement system.

Parameter	Value
Frequency band	260-320 GHz
Bandwidth	60 GHz
Time resolution	16.7 ps
Space resolution	5 mm
Sweeping interval	60 MHz
Sweeping points	1001
Maximum excess delay	16.7 ns
Maximum path length	5 m
Waveguide gain / HPBW	7 dBi / 60°
Tx-Rx distance (aligned)	0.86 m
Displacement precision	0.02 mm

TABLE II: Measurement deployment.

Scenario 1	Case 1	Case 2	Case 3
Antenna array type	16×16 UPA	32×32 UPA	64×64 UPA
Element spacing	0.5 mm	0.5 mm	0.5 mm
NF/FF region	FF	Boundary	NF

the mixed intermediate frequency (IF) signal has a frequency of 7.6 MHz. Two IF signals at Tx and Rx modules, i.e., the reference IF signal and the test IF signal, are sent back to the VNA, and the transfer function of the device under test (DUT) is calculated as the ratio of the two frequency responses. The DUT contains not only the wireless channel, but also the device, cables, and waveguides. To eliminate their influence, the system calibration procedure is conducted, which is described in detail in our previous works [23], [24].

In this measurement, we investigate the THz frequency band ranging from 260 GHz to 320 GHz, which covers a substantially large bandwidth of 60 GHz. As a result, the time and space resolution is 16.7 ps and 5 mm, respectively. The frequency sweeping interval is 60 MHz, resulting in 1001 sweeping points at each Tx-Rx position. Hence, the maximum excess delay is 16.7 ns. The corresponding maximum detectable path length is 5 m, which is sufficient for this small-scale measurement. Waveguides are integrated at both Tx and Rx modules, with gains around 7 dBi and half-power beamwidth (HPBW) around 60°.

The propagation channel is confined in a 0.69 m (length) × 0.61 m (width) × 1.00 m (depth) anechoic chamber. The inside surfaces of the chamber are wrapped by absorbing materials to restrain the multi-path effect. Tx and Rx are placed at two ends of the artificial channel. The Tx is installed on a displacement platform, which supports horizontal and vertical movements in the x - z plane perpendicular to the Tx-Rx line-of-sight. The displacement precision is 0.02 mm for both axes. The Rx is static, and the center of the Tx array is aligned with the Rx, with a distance of 0.86 m.

The PC alternately controls the movement of Tx through the displacement platform and the measuring process through the VNA. Key parameters of the measurement are summarized in Table I.

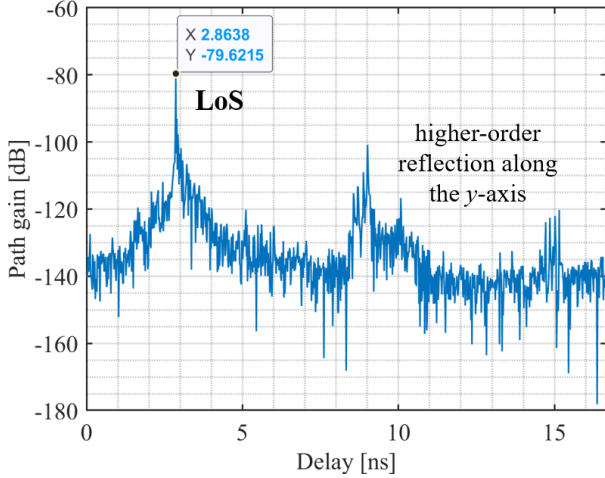


Fig. 2: CIR at the UPA center.

B. Measurement Deployment

In the measurement, as shown in Fig. 1(b), four sides of the channel are all wrapped by absorbing materials. Three cases are measured, i.e., the virtual UPA at Tx consisting of 16×16 , 32×32 , and 64×64 elements, with element spacing of 0.5 mm, as summarized in Table II.

All cases share the same center of UPA, and the Rx is perpendicularly pointing to this center. In terms of the Rayleigh distance, arrays in Case 1, 2, and 3 belong to the far-field region, far-near-field boundary, and the near-field region, respectively.

The measurement starts from the element at the left bottom corner, and all elements in the UPA are scanned first horizontally (in the x -axis) and then vertically (in the z -axis). The measuring time for each position is about 2.3 s. However, the measuring time is subject to the motion driven by the displacement platform, which takes about 4 hours to traverse a 64×64 UPA.

III. MEASUREMENT RESULTS

In this section, measurement results are discussed, including the properties of the line-of-sight (LoS) ray and the metal surface-reflected ray across the UPA in FF and NF cases. The variation of path gain and phase across the UPA is analyzed. First, we reveal non-linear phase change in the near-field region, and the Rayleigh distance in terms of the maximum phase error is verified. Second, the cross-field path loss model compatible with both FF and NF cases across the UPA structure is proposed. Besides, the multi-path fading caused by the superposition of the two rays is observed.

A. Channel impulse response

In the measurement, for each channel from one element at Tx to Rx, the frequency-domain measurement derives 1001 samples in channel transfer function (CTF), with the sample interval of 60 MHz. We then transfer it to the channel impulse response (CIR) by inverse Fourier transform (IFT), with the sample interval of 16.7 ps. We show the CIR result from the

center of the UPA to the Rx in Fig. 2. The LoS ray arrives at 2.8638 ns, corresponding to the traveling distance of 0.8591 m, and has the strongest power of 79.6 dB. The measured path loss and phase of the LoS ray across the UPA are revealed in Section III-B and Section III-C, respectively. Since the two ends of the channel are not covered by absorbing materials, we can also observe higher-order reflected rays along the y -axis.

B. Path loss

Fig. 3 shows the measured path gain of the LoS ray across the 64×64 UPA in gray dots. In the far-field region, the free-space path loss (FSPL) is given by Friis' law, which is described as

$$\text{FSPL [dB]} = 20 \times \log_{10} \frac{4\pi}{\lambda} \cdot d_{3D}, \quad (1)$$

where d_{3D} is the 3D distance between Tx and Rx, and λ represents the carrier wavelength. The Friis' law is derived from the transmission formula, which indicates how EM wave power is attenuated during its transmission between two antennas that are separated by a sufficiently large distance. The distance d_{3D} is confined to the far-field region. Therefore, Friis' law no longer works in the near-field region. For instance, in our experiment, the actual transmission distance ranges from 0.8600 m to 0.8603 m between the Rx and elements at Tx. According to the Friis' law as (1), the transmission distance corresponds to the path loss from 80.6742 dB to 80.6772 dB with variation of 0.003 dB. In contrast, the measured path loss from 79.5404 dB to 80.1555 dB with the variation of 0.6151 dB. In other words, the variation of received power at the array elements is underestimated by Friis' Law. This is attributed to the large array size compared with the small Tx-Rx distance.

Besides, in the measurement result, path gain reduces unequally along the x -axis and the z -axis. The explanation is as follows. In our experiment, standard rectangular WR2.8 waveguides are integrated onto the test port of two RF modules, which are used as open-ended waveguides (OEG) [25] with the gain around 7 dB. The gain is uniformly removed in the calibration process. However, similar to the horn antenna, whose gain decreases faster along the width (long side) than that along the height (short side) [5], gain reduction factors of the waveguide are also likely to be associated with the aperture structure, which accords with the measurement result that the path gain along the x -axis (long side) decreases more rapidly.

Instead, inspired by the expression of antenna aperture gain in the NF [5], we propose a cross- far- and near-field path loss model for the MISO system with the UPA structure, by introducing a cross-field factor K , as

$$\text{PL [dB]} = 20 \times \log_{10} \frac{4\pi}{\lambda} \cdot d_{\text{ref}} \cdot K(\Delta x, \Delta z, \lambda, d_0), \quad (2a)$$

$$K(\Delta x, \Delta z, \lambda, d_0) = 1 + C_1 \frac{\left(\frac{\Delta x}{C_3}\right)^2 + \left(\frac{\Delta z}{C_4}\right)^2}{\lambda} - C_2 \cdot d_0, \quad (2b)$$

where the reference distance d_{ref} is a model parameter. K is the cross-field factor associated with the coordinate of the element relative to the center (Δx , Δz), the wavelength λ , and the distance from the UPA center to the Rx d_0 .

The proposed model provides a statistical way to characterize the power change across the UPA at a fixed Tx-Rx distance, whereas the parameters are designed to imply physical meanings. Starting at the center of the array (when $\Delta x = \Delta z = 0$), the absolute value of power is first corrected by introducing parameter d_{ref} . Then, as we move to another position ($\Delta x, \Delta z$) away from the center, it turns to the question whether the movement is prominent compared with the Tx-Rx distance d_0 , which is equivalent to the question whether the array at d_0 with aperture size $\sqrt{\Delta x^2 + \Delta z^2}$ is in the NF region. Therefore, the cross-field factor K is used to revise the implementation of Friis' Law in the NF region, which increases when the NF effect becomes more significant by (i) the expansion of the UPA compared with the wavelength, (ii) the decrease of the Tx-Rx distance, and (iii) the relative degree between the above two factors.

In the expression of the cross-field factor K , parameter C_1 is the base of the exponential function C_1^p , where the exponent $p = \left[\left(\frac{\Delta x}{C_3} \right)^2 + \left(\frac{\Delta z}{C_4} \right)^2 \right] / \lambda - C_2 \cdot d_0$ maps the obscure transition between FF and NF to the value of factor K . The value of C_1 is larger than 1 so that (i) C_1^p and K increase with p , i.e., when the UPA expands, the correction factor K becomes more significant, and (ii) $C_1^p \rightarrow 0$ and $K \rightarrow 1$ as p decreases. At the UPA center, $\Delta x = \Delta z = 0$, and the path loss is equal to the Friis' FSPL at the equivalent distance $d_{\text{ref}} \cdot (1 + C_1^{-C_2 \cdot d_0})$.

Furthermore, as the distance from the UPA center to the Rx d_0 is fixed, C_2 adjusts the transition between FF and NF. For instance, in this measurement, Rx is pointing perpendicular to the UPA, i.e., the spatial angle at the UPA center is $\theta = 0^\circ$. In a general MISO model, the Rayleigh distance is proportional to the square of $\cos \theta$. Specifically, according to the more universal formula of the Rayleigh distance that consists of the spatial angle, $2D^2(\cos \theta)^2/\lambda$, when the UE points to the UPA center with a larger spatial angle to the UPA plane, the NF effect is less significant. Though the angle θ is not included in the model, it is already embodied in values of C_2, C_3 and C_4 . Besides, parameters C_3 and C_4 are intended to model the different degrees of path loss descent along two axes.

Fig. 3 shows the fitting result of the measured path gain across the UPA, with the mean squared error (MSE) of 0.0022. The result is discussed as follows. First, $d_{\text{ref}} = 0.4459$, $C_1 = 1.3295$, $C_2 = 1.1433$, and the path loss at the UPA center given by the model is 79.56 dB, equivalent to the Friis' FSPL at $d_{\text{ref}} \cdot (1 + C_1^{-C_2 \cdot d_0}) = 0.7829$ m. Second, $C_3 = 0.8885$ and $C_4 = 1.2318$, which accords with the measurement result where the path loss decreases more rapidly along the x -axis, compared with the counterparts along the z -axis. Thanks to the cross-field factor, the proposed path loss model is accurate across NF and FF regions.

C. Phase

Table III summarizes the phase change along horizontal (x -axis) and vertical (z -axis) positions. Colored lines indicate phase change among horizontal/vertical elements at different vertical/horizontal positions. In the FF case, the maximum phase difference across each column and each row

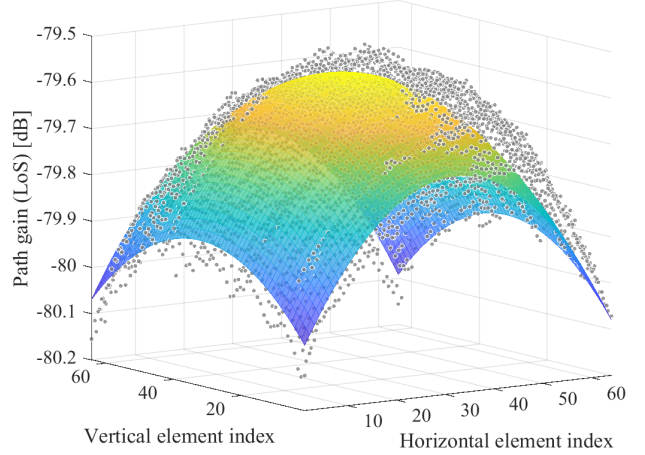


Fig. 3: Path gain of the LoS ray across the UPA. Gray dots represent the measurement result, and the colored surface represents the model fitting result.

TABLE III: Phase of the LoS ray across the UPA.

Phase change $\Delta\phi$ among horizontal elements	Phase change $\Delta\phi$ among vertical elements
Case 1: 16×16 UPA, Far-field	
$\Delta\phi \leq 0.2840 < \pi/8$	$\Delta\phi \leq 0.1713 < \pi/8$
Case 2: 32×32 UPA, Far-near-field boundary	
$\pi/8 < 0.7476 \leq \Delta\phi \leq 0.7875$	$\Delta\phi \leq 0.3166 < \pi/8$
Case 3: 64×64 UPA, Near-field	
$\Delta\phi > \pi$	$\Delta\phi > \pi$

are both smaller than $\pi/8$, which accords with the definition of Rayleigh distance and can be regarded as a linear phase change. When the UPA expands to 32×32 in Case 2 and 64×64 in Case 3, the phase difference gradually exceeds $\pi/8$, and a non-linear phase change can be clearly observed. In particular, the phase change among vertical elements is less smoother, since the measurement scans the UPA first in the x -axis and then in the z -axis. In other words, the measurement at vertical elements is not continuous and is affected by the positional accuracy of the displacement platform.

IV. CONCLUSION

In this paper, we conducted a wideband MISO channel measurement with a virtual planar array at 260-320 GHz. Channels from at most 4096 elements in the UPA are investigated. The characteristics of far- and near-field channels across the UPA are elaborated. Specifically, properties of LoS and surface-reflected rays across the UPA are analyzed, and the following observations are drawn. First, non-linear phase change is observed in the NF region, and the Rayleigh criterion regarding the maximum phase error is verified. Second, instead of Friis' formula, a new cross-field path loss model compatible with both FF and NF cases across the UPA structure is proposed. Specifically, a cross-field factor is parameterized in the model to reveal the transition between FF and NF cases, which is determined by the squared distance between the element and the UPA center, the carrier wavelength, and the UPA center-Rx distance. At this stage, the proposed model is statistically accurate and has a physical meaning. The structure of the model can be generalized to other distances. Still, more measurements and further analysis at different Tx-Rx distances (d_0) and frequencies (f , or wavelength λ) are essential, in order to make a conclusion on model parameters.

REFERENCES

- [1] I. F. Akyildiz and J. M. Jornet, "Realizing ultra-massive MIMO (1024×1024) communication in the (0.06–10) terahertz band," *Nano Communication Networks*, vol. 8, pp. 46–54, 2016.
- [2] M. Cui, Z. Wu, Y. Lu, X. Wei, and L. Dai, "Near-field MIMO communications for 6G: Fundamentals, challenges, potentials, and future directions," *IEEE Communications Magazine*, vol. 61, no. 1, pp. 40–46, 2022.
- [3] C. Han, Y. Wang, Y. Li, Y. Chen, N. A. Abbasi, T. Kürner, and A. F. Molisch, "Terahertz Wireless Channels: A Holistic Survey on Measurement, Modeling, and Analysis," *IEEE Communications Surveys & Tutorials*, vol. 24, no. 3, pp. 1670–1707, Jun. 2022.
- [4] K. T. Selvan and R. Janaswamy, "Fraunhofer and Fresnel Distances: Unified derivation for aperture antennas," *IEEE Antennas and Propagation Magazine*, vol. 59, no. 4, pp. 12–15, 2017.
- [5] L. Xiao, Y. Xie, P. Wu, and J. Li, "Near-Field Gain Expression for Aperture Antenna and Its Application," *IEEE Antennas and Wireless Propagation Letters*, vol. 20, no. 7, pp. 1225–1229, 2021.
- [6] P. Kaurav, S. K. Koul, and A. Basu, "Determination of Near Field Path Loss in Millimeter Wave Spectrum," in *Proc. of IEEE MTT-S International Microwave and RF Conference (IMARC)*, pp. 1–4, 2019.
- [7] S. Sun, R. Li, X. Liu, L. Xue, C. Han, and M. Tao, "How to Differentiate between Near Field and Far Field: Revisiting the Rayleigh Distance," *arXiv preprint arXiv:2309.13238*, 2023.
- [8] Z. Zhou, X. Gao, J. Fang, and Z. Chen, "Spherical Wave Channel and Analysis for Large Linear Array in LoS Conditions," in *Proc. of IEEE Globecom Workshops (GC Wkshps)*, pp. 1–6, 2015.
- [9] Y. Chen, L. Yan, and C. Han, "Hybrid Spherical- and Planar-Wave Modeling and DCNN-Powered Estimation of Terahertz Ultra-Massive MIMO Channels," *IEEE Transactions on Communications*, vol. 69, no. 10, pp. 7063–7076, 2021.
- [10] L. Li, H. Li, Z. Chen, W. Chen, and S. Li, "An Analytical Range-Angle Dependent Beam Focusing Model for Terahertz Linear Antenna Array," *IEEE Wireless Communications Letters*, vol. 11, no. 9, pp. 1870–1874, 2022.
- [11] M. Cui and L. Dai, "Channel Estimation for Extremely Large-Scale MIMO: Far-Field or Near-Field?" *IEEE Transactions on Communications*, vol. 70, no. 4, pp. 2663–2677, 2022.
- [12] Y. Xie, B. Ning, L. Li, and Z. Chen, "Near-Field Beam Training in THz Communications: The Merits of Uniform Circular Array," *IEEE Wireless Communications Letters*, vol. 12, no. 4, pp. 575–579, 2023.
- [13] G. Bacci, L. Sanguinetti, and E. Björnson, "Spherical Wavefronts Improve MU-MIMO Spectral Efficiency When Using Electrically Large Arrays," *IEEE Wireless Communications Letters*, vol. 12, no. 7, pp. 1219–1223, 2023.
- [14] K. Chen, C. Qi, C.-X. Wang, and G. Y. Li, "Beam training and tracking for extremely large-scale mimo communications," *IEEE Transactions on Wireless Communications*, pp. 1–1, 2023.
- [15] K. Chen, C. Qi, O. A. Dobre, and G. Y. Li, "Triple-refined hybrid-field beam training for mmwave extremely large-scale mimo," *IEEE Transactions on Wireless Communications*, pp. 1–1, 2024.
- [16] S. Wu, C.-X. Wang, H. Haas, E.-H. M. Aggoune, M. M. Alwakeel, and B. Ai, "A Non-Stationary Wideband Channel Model for Massive MIMO Communication Systems," *IEEE Transactions on Wireless Communications*, vol. 14, no. 3, pp. 1434–1446, 2015.
- [17] A. Ali, E. D. Carvalho, and R. W. Heath, "Linear receivers in non-stationary massive mimo channels with visibility regions," *IEEE Wireless Communications Letters*, vol. 8, no. 3, pp. 885–888, 2019.
- [18] X. Cheng, K. Xu, J. Sun, and S. Li, "Adaptive Grouping Sparse Bayesian Learning for Channel Estimation in Non-Stationary Uplink Massive MIMO Systems," *IEEE Transactions on Wireless Communications*, vol. 18, no. 8, pp. 4184–4198, 2019.
- [19] Y. Han, S. Jin, C.-K. Wen, and X. Ma, "Channel estimation for extremely large-scale massive mimo systems," *IEEE Wireless Communications Letters*, vol. 9, no. 5, pp. 633–637, 2020.
- [20] S. Payami and F. Tufvesson, "Channel measurements and analysis for very large array systems at 2.6 GHz," in *Proc. of European Conference on Antennas and Propagation (EUCAP)*, pp. 433–437, 2012.
- [21] A. O. Martinez, E. De Carvalho, and J. Ø. Nielsen, "Towards very large aperture massive MIMO: A measurement based study," in *Proc. of IEEE Globecom Workshops (GC Wkshps)*, pp. 281–286, 2014.
- [22] Z. Yuan, F. Zhang, Y. Zhang, J. Zhang, G. F. Pedersen, and W. Fan, "On Phase Mode Selection in the Frequency-Invariant Beamformer for Near-Field mmWave Channel Characterization," *IEEE Transactions on Antennas and Propagation*, vol. 71, no. 11, pp. 8975–8986, 2023.
- [23] Y. Wang, Y. Li, Y. Chen, Z. Yu, and C. Han, "0.3 THz Channel Measurement and Analysis in an L-shaped Indoor Hallway," in *Proc. of IEEE ICC*, pp. 1–6, Jun. 2022.
- [24] Y. Li, Y. Wang, Y. Chen, Z. Yu, and C. Han, "Channel Measurement and Analysis in an Indoor Corridor Scenario at 300 GHz," in *Proc. of IEEE ICC*, pp. 1–6, Jun. 2022.
- [25] S. Kawalko and M. Kanda, "Near-zone gain of open-ended rectangular waveguides," *IEEE Transactions on Electromagnetic Compatibility*, vol. 39, no. 4, pp. 408–413, 1997.